Analysis of Vortex Ingestion Impact on the Dynamic Response of the Fan in Resonance Condition

Thomas Berthelon, Alain Dugeai, Jonathan Langridge, Fabrice Thouverez

Analysis of vortex ingestion impact on the dynamic response of the fan in resonance condition

Thomas Berthelon, Safran Aircraft Engines
thomas.berthelon@safrangroup.com

Alain Dugeai,ONERA
alain.dugeai@onera.fr

Jonathan Langridge, Safran Aircraft Engines

Fabrice Thouverez, Ecole Centrale de Lyon
fabrice.thouverez@ec-lyon.fr

2019

Abstract

Ultra high by-pass ratio (UHBR) turbofan configurations are promising concepts to address the issue of aircraft fuel burn reduction. The large fan diameter and the small ground clearance of these configurations can lead to ingestion of ground vortex during take-off phases. This vortex can be responsible of high level of vibrations and possible failure due to high cycle fatigue. The objective of the work described in this paper is to investigate the forced response due to ground vortex ingestion of a large civil fan in resonance condition. This paper is separated in three sections. The first one consists of characterizing the flow distortion induced by a ground vortex. The second part consists of evaluating the blade vibrations induced by this vortex with decoupled aeromechanical method. The numerical predictions are then compared to experimental results. And finally, the last part consists of proposing a low fidelity model based on swirl distortion in order to estimate modal aerodynamic forces in ground vortex ingestion case.

INTRODUCTION

A vortex can form under certain conditions when the intake of an engine is situated near the ground surface. This vortex may stretch from the surface into the

inlet causing significant flow distortions. The vortex becomes visible in a rainy or humid day because the moisture at its core condenses. This ground vortex can lead to ingestion of loose debris [16] and excessive blade vibrations [5] [7]. This paper deals with the second point. The mechanisms of inlet vortex formation have been a popular subject of research since the 1950s. It was quickly identified that a necessary requirement for vortex formation is the existence of a stagnation point on the ground plane [16]. De Siervi et al.[4] suggested that there might be two different mechanisms of inlet vortex generation. The first of these is the amplification of ambient vorticity as the vortex lines are stretched and drawn into the inlet under headwind conditions. The second mechanism is that an inlet vortex can arise in an upstream irrotational flow, for an inlet in crosswind, which does not require the presence of ambient vorticity. The parameters that can be used to characterize this phenomenon are the velocity ratio of inlet velocity to ambient velocity, the ratio of inlet height to inlet diameter [4][18]. More recently, Murphy [13] proposed a series of experimental studies involving the effect of ground clearance, yaw angles and intensity of incoming wind or even the ambient boundary layers size. The first section of this paper consists of characterizing the aerodynamic distortion induced by a ground vortex. The flow field around the intake of a large civil turbofan operating near the ground is predicted with a 3D-RANS approach.

A frequent cause of turbomachinery blade failure is excessive resonant response. The standard method for dealing with this problem is to avoid resonant conditions using a Campbell diagram. Unfortunately, it is impossible to avoid all resonant conditions, especially during the take-off phases where the ground vortex can appear. Previous studies from Green [7] and Di Mare et al. [5] showed that the ingested inlet ground vortex could lead to a large increase in the fan forced resonant response. During the last decades, several numerical approaches have been developed to predict forced response. A classification of these approaches can be found in literature [10]. The coupled approach consists in coupling the fluid and the structure at each time step. Although being the most representative approach, the coupled approach is very expensive due to the long time to converge to periodic state. For blade forced responses, the decoupled approach based on the superposition principle is often preferred because it is less computationally expensive and gives similar results compared to the coupled approach [9] [17] [12]. The second part of this paper consists in evaluating the vibration response of the fan blade, due to ground vortex ingestion. The dynamic response in resonance condition are computed with a decoupled approach using linear representation of the structure and aerodynamic U-RANS computations. The numerical results are compared to the experimental data available.

By analyzing distortion coming from vortex ingestion, Di Mare shows that there is no linear correlation between the amplitudes of the distortion harmonics and the resulting vibratory response of the blades [5]. The last part of this paper consists in proposing a model to connect the forced response to the distortion map. This model aims to compute the generalized aerodynamic forces thanks to swirl distortion maps, geometrical features and blade mode-shape of the blade.

Such a model allows a better understanding of the way the vortex excites the blade.

INLET GROUND VORTEX DISTORTION

The MASCOT 2 configuration

MASCOT 2 is a Safran Aircraft Engines full-scale turbofan demonstrator for modern aero-engines. This demonstrator has been tested through a complete experimental campaign, including performance, acoustics, operability and cross-wind tests. It provides a valuable database to validate simulation models. In this paper we focus on the cross-wind tests where the fan blade vibrations were measured both with and without ground. During these tests, no information about the flow field around the intake or on the distortion inside the intake is available. Unfortunately for this full scale industrial test, no performance map is available, nor detailed blade pressure blade measurements (no kulites).

Numerical setup

The three-dimensional flow field was predicted with elsA(ONERA-Airbus-Safran property)[2] based on the solution of the RANS equations for a compressible and ideal gas. Spatial discretisation was performed using AUSM+(P) scheme[11]. The turbulence model $k-\omega$ of Menter with SST correction is used. Sereval authors obtained good results in ground vortex prediction with this model [21],[3]. This model has been validated against experimental data from an academic case in previous study [1]. The overall computational domain consists of a rectangular prism with length and height of 10 D_l and width and 20 D_l width. The diameter D_l represents the highlight diameter. The ground clearance is set at $h/D_l = 0.35$ where h represents the distance between the ground and the lower point of the highlight plane. The upstream boundary is specified as a pressure inlet. The downstream boundary implements a pressure outlet condition where the pressure is specified to deliver the required crosswind with an angle of 90°. There is no fan in this model, the suction flow is generated by a pressure outlet condition inside the intake. Adding the fan could allow to capture the coupling between the fan and the ground vortex, however it will force to perfom an unsteady simulation which will be much more time consumming. Such a computation will be adressed in a futur study. This numerical methodology has been validated against experimental data from an academic case in previous study [1]. The velocity ratio V_i/V_∞, resulting from the crosswind and the mass flow studied, is close to 13. Considering the value of h/D_l and V_i/V_∞ in this case, the ground presence implies a formation of a ground vortex ingested into intake.

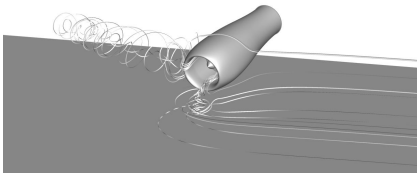

Figure 1: FLOW FIELD TOPOLOGY IN MASCOT2 CASE.

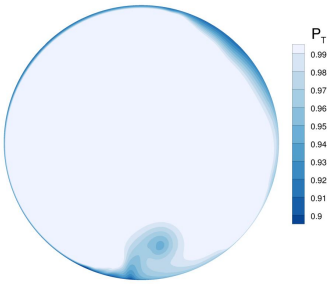

Figure 2: TOTAL PRESSURE MAP.

Results

The flow topology is depicted on Fig. 1 where streamlines of the ground vortex and the trailing vortex are illustrated. The total pressure distortions obtained inside the intake are presented in Fig. 2. The total pressure loss induced by the ground vortex is easily visible in the lower part of the pressure field. The zone of pressure distortion is localized in a very confined space at high radius. Another total pressure distortion is present for high radius at the upper part. This distortion comes from the ingestion of the trailing vortex illustrated in Fig. 1.

In order to characterize the distortion induced by the ground vortex it is interesting to look at the swirl angle, defined in Eq. 1.

$$\alpha = atan(\frac{v_t}{v_x}) \tag{1}$$

The swirl angle distortions is presented Fig. 3. The azimuthal variation of the swirl angle gives an idea of the variation of the blade angles of attack during the rotation and therefore the variation of aerodynamic forces which will impact forced response. The vortex leads to two large zones of swirl angle distortion: one near the shroud with negative swirl angles and one for lower radius with positive swirl angles. Contrary to the total pressure distortion, the swirl distortion impacts a large radial area. At the vortex core, where the total pressure drop is

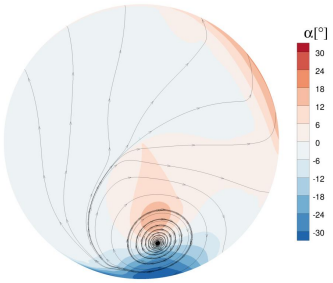

Figure 3: SWIRL ANGLE MAP.

the highest, the swirl angle is very low, because tangential velocity is near zero in this region. In conclusion, for this turbofan configuration, the ground vortex leads to a very localized total pressure drop and strong positive and negative swirl angles.

DECOUPLED APPROACH FOR THE FORCED RESPONSE OF FAN BLADES

Structural modelling

In this study, the behaviour of the structure is assumed to be linear. The blade displacement u_{disp} can be expressed in the modal base Φ with the generalized coordinates q.

$$u_{disp} = \Phi q \tag{2}$$

The modal dynamical equation for the aeromechanical system is expressed with the modal mass matrix μ, modal mechanical damping matrix β_{mech}, modal stiffness matrix γ and generalized aerodynamic forces G_{af}, which are the aerodynamic forces projected on the modal base, in Eq. 3.

$$\mu\ddot{q} + \beta_{mech}\dot{q} + \gamma q = G_{af} \tag{3}$$

The finite element structural model used is classically a single sector of disk and fan blade. A static computation is first made including centrifugal effects and static aerodynamic pressure. The shape and characteristics of the modes are obtained by a modal analysis including cyclic symmetrical conditions [19] [8]. The complex mode shape obtained on the reference blade is recombined on the whole row using cyclic symmetrical properties. The full annulus complex mode is separated into two real modes ϕ' and ϕ'' as it is illustrated on Fig. 4 for the second bending mode and the nodal diameter 4. These two real modes have

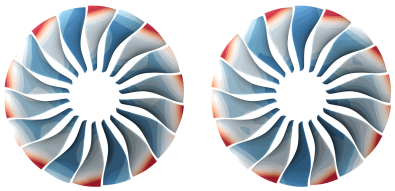

Figure 4: TANGENTIAL DISPLACEMENT OF THE 2F-4/rev MODE-SHAPE. LEFT : ϕ', RIGHT : ϕ''.

the same frequency and the same generalized mass. The present study aims to compute the response at the 2F-4/rev crossing therefore the modal base can be reduced to only these two modes. The combination of these two real modes allows describing direct and indirect rotating waves. The mechanical damping β_{mech} is neglected in this study because the only data available during tests is the aero-mechanical damping which includes both aerodynamic and structural damping.

Aerodynamic calculation

Aerodynamic calculations are performed using U-RANS modeling with elsA (ONERA-Airbus-SAFRAN property)[2]. Arbitrary Lagrangian-Eulerian formulation (ALE) is used to take into account the deformation of the mesh at each time step [15] [6]. The Jameson scheme is used as spatial discretisation. The turbulence model $k-\omega$ of Menter with SST correction is used. The temporal discretisation is achieved by a GEAR scheme with 15 dual iterations. 720 times steps per revolution are performed. The model used for aerodynamic calculations includes the 18 fan blades, a splitter and only one OGV. The domain is illustrated in Fig. 5 and contains more than 50 million cells. The secondary flow exit is controlled by a static pressure outlet and a radial equilibrium condition. Azimuthal averaged mixing condition is applied between the OGV and the fan. This simplification allows to save computational cost by modeling only one OGV. The fan forcing due to the OGV is therefore not taken into account but this forcing is expected small compared the forcing due to the inlet vortex. The primary flow exit is also controlled by outlet static pressure prescription using a radial equilibrium condition. A condition of injection is applied at the inlet. Total pressure, total enthalpy, velocity vector and turbulent variables are directly interpolated from the intake calculations presented in the previous section. For the 8 first cells the flow is resolved in the absolute frame before being resolved in the relative frame thanks to a sliding mesh condition (replaced by a mixing plane for steady initialization calculations). The inlet condition is close to the fan and may impact the results. In order to get rid of this problem, a simulation included the intake and the fan has to be done. However, such a simulation has a higher computational cost. The mode shapes are interpolated onto the fan

Figure 5: CFD DOMAIN

aerofoil surface in the CFD model. Only the two real mode shapes ϕ' and ϕ'' are embedded in this study because the forced response on the 2F-4/rev is driven by these modes.

Decoupled approach

The decoupled approach is based on the superposition principle which consists in separating the generalized aerodynamic forces induced by the distortion, G^f_{af}, and the damping generalized aerodynamic forces induced by vibrations, G^d_{af}, as it is illustrated Eq.4:

$$\mu\ddot{q} + \gamma q = G^d_{af}(q, \dot{q}) + G^f_{af} \tag{4}$$

The damping generalized aerodynamic forces are assumed linear with the displacement and the velocity. This assumption is generally valid for turbomachinery blades which are of high density and stiffness and vibrate at low amplitudes. Finally, the displacement of the blades is described by the Eq. 5 where A is the aerodynamic stiffness matrix and B the aerodynamic damping matrix.

$$\mu\ddot{q} + \gamma q = Aq + B\dot{q} + G^f_{af} \tag{5}$$

By considering only the complex mode 2F with a nodal diameter of 4 (ϕ' and ϕ''), the system defined in Eq. 5 is reduced to only two real equations coupled by aerodynamic matrices A and B.

Usually, the excitation forces (G^f_{af}) and the aerodynamic response to motion (G^d_{af}) are evaluated through two individual CFD computations. The excitation forces G^f_{af} are estimated using a stage computation (distortion + fan) with the assumption of the blade-motion-independence. The aerodynamic matrices A and B are obtained by performing the computation in a clean flow (without the distortion) with a prescribed forced harmonic motion [12] [17]. In this study a different approach has been used to estimate A,B and G^f_{af}. Two computations are made with the distortion and a prescribed harmonic motion. Such

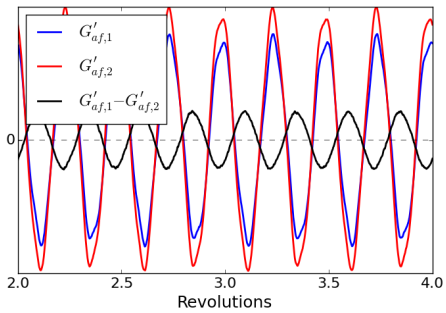

Figure 6: EVOLUTION OF GENERALIZED AERODYNAMIC FORCES G'_{af} FOR TWO TWIN COMPUTATION.

a computation can be called *twin computation*. The only difference between these two twin computations is the amplitude and the phase chosen for the prescribed harmonic motion. The analysis of the temporal generalized aerodynamic forces allows to extract A and B and therefore to build G^f_{af}. The interest of this approach is to keep the same numerical method for both computations and therefore avoid modelling issues due to the modification of boundary conditions. Moreover, it simplifies the set up compared to the classical approach that requires two different setups. However, it must be noticed that this approach still relies on a linear superposition principle. In order to explain the process, we will focus on single degrees of freedom but it is easily transposable to the two real modes case resulting of the cyclic symmetry properties. Two computations, indexed by 1 and 2, with two prescribed motion with an amplitude of q, a phase ψ and the same pulsation ω (which is 4 times the pulsation of the rotating pulsation in a case of a 4/rev crossing) are considered. The two amplitudes are chosen close to the amplitude observed during test. These two prescribed motions are expressed in Eq. 6:

$$\begin{aligned} q_1 &= q_1^* cos(\omega t + \psi_1) \\ q_2 &= q_2^* cos(\omega t + \psi_2) \end{aligned} \tag{6}$$

An example of the evolution of the generalized aerodynamic force of mode ϕ' is illustrated in Fig. 6 for two different twin computations with different amplitude of prescribed motion. Thanks to superposition and linear assumptions, the generalized aerodynamic forces can be written as a function of aerodynamic matrix and generalized aerodynamic forces due to the distortion, as shown in Eq. 7

$$\begin{aligned} G_{af,1} &= Aq_1^* cos(\omega t + \psi_1) - \omega B q_1^* sin(\omega t + \psi_1) + G^f_{af} \\ G_{af,2} &= Aq_2^* cos(\omega t + \psi_2) - \omega B q_2^* sin(\omega t + \psi_2) + G^f_{af} \end{aligned} \tag{7}$$

A Fourier analysis of the difference between the two G_{af} is then carried out and leads to Eq. 8 where Re represents the real part and Im the imaginary part.

$$\frac{2}{T}\int_0^T (G_{af,1} - G_{af,2})e^{-j\omega t}dt = Re + jIm \tag{8}$$

Then, by replacing $G_{af,1}$ and $G_{af,2}$ by their expression in Eq. 7, the Fourier analysis can be written as shown in Eq. 9.

$$\begin{gathered}\frac{2}{T}\int_0^T (G_{af,1} - G_{af,2})e^{-j\omega t}dt = \\ A(q_1^* cos(\psi_1) - q_2^* cos(\psi_2)) + \omega B(q_2^* sin(\psi_2) - q_1^* sin(\psi_1)) + \\ j[A(q_1^* sin(\psi_1) - q_2^* sin(\psi_2)) + \omega B(q_1^* cos(\psi_1) - q_2^* cos(\psi_1))]\end{gathered} \tag{9}$$

The identification of Re and Im and the real and imaginary part of Eq. 9 leads to a 2x2 system where the unknowns are A and B (which are scalar in the one degree of freedom case). Once the system is solved, the generalized aerodynamic forces induced by the distortion G_{af}^f are obtained by subtracting the generalized aerodynamic forces due to motion to the total generalized aerodynamic forces (see Eq. 7). In the case of the two real modes ϕ' and ϕ'' from the cyclic symmetries formulation, two twin computations are made by imposing motion on the mode ϕ'. In view of the properties of aerodynamic matrices A and B due to cyclic symmetry properties, the Fourier analysis leads to a 4x4 system allowing the determination of the aerodynamic matrices. In the same way, the generalized aerodynamic forces due to distortion $G_{af} = [G_{af}^{f'}, G_{af}^{f''}]^T$ are obtained by subtracting the part due to motion to the total generalized aerodynamic forces (see Eq. 7). At a resonance condition, the displacement and therefore the generalized coordinates are assumed harmonic with a pulsation ω. The generalized coordinate can be written thanks to the complex number $\widehat{q'}$ and $\widehat{q''}$ as illustrated in Eq.10.

$$q = [\widehat{q'}e^{j\omega t}, \widehat{q''}e^{j\omega t}] \tag{10}$$

The system of the Eq. 5 can thus be written in frequency domain via a Fourier analysis as shown in Eq. 11.

$$\begin{gathered}(\gamma - A - \omega^2\mu - j\omega B)[\widehat{q'}, \widehat{q''}]^T = \\ \frac{2}{T}\int_0^T [G_{af}^{f'}, G_{af}^{f''}]^T e^{-j\omega t}dt\end{gathered} \tag{11}$$

The complex generalized coordinates $\widehat{q'}$ and $\widehat{q''}$ are then obtained by inverting the system. Eq. 11 is valid only at the frequency computed in twin calculations. However, for a range of frequencies close to this frequency, the aerodynamic behaviour is assumed to stay the same. In the context of steady excitation in

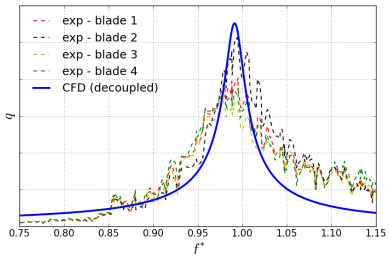

Figure 7: FORCED RESPONSE FOR THE 2F-4/REV CROSSING, NUMERICAL PREDICTION AGAINST EXPERIMENTAL DATA.

the absolute frame, the resolution leads to the same amplitude and a 90° phase-shift for the modes ϕ' and ϕ'', which describes an indirect rotating wave in the relative frame.

Results

The cross-wind tests consist in a slow increase in rotating speed from idle speed to the maximum speed of the engine. During this cross-wind test, no information on the performance of the engine is available. Four fan blades are instrumented with strain gauges during cross-wind study of MASCOT2 campaign test. The gauges used are mainly sensitive to the second bending mode. In order to extract the component induced by the crossing 2F-4/rev in the strain gauge measurements, the 4^{th} engine order signal is selected thanks to a sliding Fourier transformation. The measured data are then converted into generalized coordinate levels thanks to the comparison with the normalized stress extracted during the modal analysis. The numerical predictions of the generalized coordinate amplitude are compared to the experimental results obtained on the fourth blade instrumented during the cross-wind study on Fig. 7. The discrepancy between the four gauges suggests that mistunning plays a role in the forced response. The mistunning is not taken into account in the numerical approach which is based on cyclic symmetry properties. A good agreement is nevertheless obtained between numerical prediction and experimental results who lead to close levels of magnitude. The levels at resonance are over-estimated by the numerical model (at least for 3 blades). An explanation can be found by the fact that the mechanical damping is neglected in the numerical approach. Indeed, the addition of a mechanical damping will lead to a decrease of maximum level reached at the resonance. Unfortunately, the value of the mechanical damping of this industrial configuration is unknown.

ESTIMATION OF AERODYNAMIC FORCES BASED ON SWIRL DISTORTION

This section aims at proposing a new model allowing the computation of the generalized aerodynamic forces induced by the ground vortex. This work is part of the decoupled approach framework presented in the second section of this paper. The objective is to estimate G_{af}^{f} (see Eq. 4) only by considering the swirl distortion map and geometrical features of the fan using drastic assumptions on the aerodynamic model.

Model description

Flow deflection in cascade of aerofoils.

In order to estimate the force produced by a rotor in a design process, it is standard to consider the flow-deflecting of a cascade of aerofoils depicted in Fig. 8. For incompressible, two-dimensional, periodic and stationary flow, the mass conservation equation applied on the dotted surface in Fig. 8 leads to the axial velocity conservation illustrated in Eq. 12.

$$u_{x1} = u_{x2} \tag{12}$$

With the same hypothesis, the momentum conservation links the axial f_X and the tangential f_T force components per unit span to the tangential velocity upstream u_{t1} and downstream u_{t2}, the density ρ and the pitch $s = 2\pi r/N_{blade}$ as shown in Eq. 13.

$$\begin{aligned} f_X &= \frac{dF_X}{dr} = \frac{1}{2}\rho s(u_{t2}^2 - u_{t1}^2) \\ f_T &= \frac{dF_T}{dr} = \rho s u_x(u_{t1} - u_{t2}) \end{aligned} \tag{13}$$

Tangential velocities, u_{t1} and u_{t2}, are directly linked to the axial velocity u_x and angles β_1 and β_2 as illustrated in Fig. 8. The outlet flow is assumed to make angle δ with the local tangents β_{sk2} as shown in Eq. 14.

$$\beta_2 = \beta_{sk2} + \delta \tag{14}$$

Wallis [20] proposed to estimate δ by a function of the chord c, the camber angle $\kappa = \beta_{sq1} - \beta_{sk2}$ and s as shown in Eq. 15.

$$\delta = 0.26\kappa\sqrt{\frac{s}{c}} \tag{15}$$

If the incoming flow is known, aerodynamic forces applied on the aerofoil can be estimated by considering key features of the blade geometry.

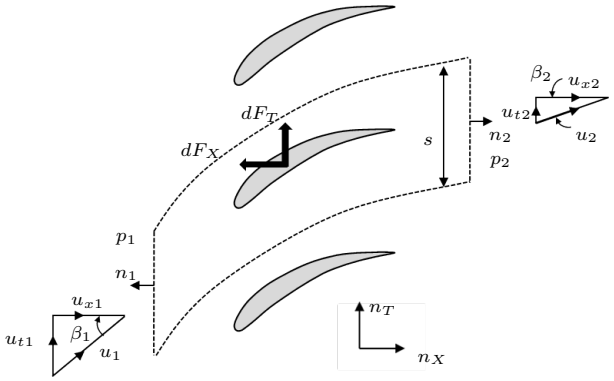

Figure 8: FLOW DEFLECTION IN CASCADE OF AEROFOIL.

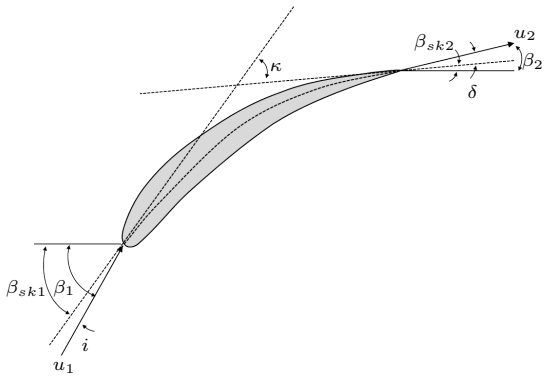

Figure 9: DETAILS OF AEROFOIL ANGLES.

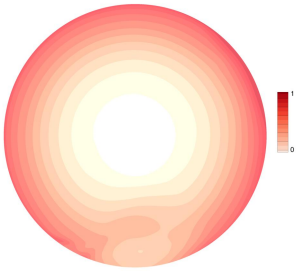

Figure 10: MODEL ESTIMATION OF THE AERODYNAMIC FORCES MAP NORMALIZED ($|\underline{f}^*_{aero}|$).

Generalized aerodynamic forces computation.

We consider a distortion map coming from an intake computation presented in the first section of this paper. This distortion map is characterized by the density $\rho(r,\theta)$ and the absolute velocity $\underline{v}(r,\theta)$. The relative velocity $\underline{u_1}$ in front of the fan is computed with the knowledge of the rotational speed Ω as explained in equation Eq. 16 :

$$\underline{u_1} = (u_{x1}, u_{r1}, u_{t1})^T = (v_x, v_r, v_t - \Omega r)^T \tag{16}$$

Moreover, with the knowledge of the number of blade N_{blade} and radial geometric characteristics of the blade $c(r)$, $\beta_{sq1}(r)$, $\beta_{sq2}(r)$, the forces $f_X(r,\theta)$ and $f_T(r,\theta)$ are computed thanks to Eq. 13, 14 and 15. The aerodynamic forces per unit span vector applied on the aerofoil is named f_{aero} and defined by Eq. 17. Its norm is illustrated in Fig. 10 for the distortion presented Fig. 3.

$$\underline{f}_{aero} = (f_X, f_T, 0)^T \tag{17}$$

For each azimuth position θ of the map, the model estimates the radial distribution of the aerodynamic force on the blade. And therefore, by traveling though θ at the rotational speed Ω (i.e. $\theta = \Omega t$), the map represents the temporal evolution of aerodynamic forces occurring on the blade. In order to compute the G^f_{af}, only a radial evolution of the mode is needed, i.e. 1-D mode-shape. According to the thin aerofoil theory, fluctuations of aerodynamic forces are applied on the quarter-chord point that is why the choice is made to reduce the 2-D mode-shape to its value on the quarter-chord line, $\phi^{c/4}$. This assumption can be very dangerous for torsion modes, because the quarter-chord line can be close to a nodal line. For bending modes, this assumption seems less dangerous because the mode-shape does not vary a lot in the axial direction. In this section, all the modes considered are complex due to single sector (S_0) reduction. Moreover, the mode-shapes are considered constant with the nodal diameter. The complex generalized aerodynamic forces of mode i on blade S_0

are then computed by summing each radial contribution as shown Eq. 18.

$$G^f_{af,i}(S_0,t) = \int_{r_{min}}^{r_{max}} \overline{\underline{\phi_i^{c/4}}}(r).\underline{f}_{aero}(r,\Omega t)dr \tag{18}$$

And finally, the harmonic generalized aerodynamic force for the mode i and the nodal diameter N_D on the whole row, $\hat{G}^{f,N_D}_{af,i}$, is obtained thanks to cyclic symmetry properties by multiplying by the number of blade N_{blade} and by performing a Fourier transformation as illustrated Eq. 19 [1].

$$\hat{G}^{f,N_D}_{af,i} = N_{blade}\frac{2}{T}\int_0^T G^f_{af,i}(S_0,t)e^{-jN_D\Omega t}dt \tag{19}$$

Reference computation

In order to evaluate the model proposed, a high fidelity computations are performed with the code elsA (ONERA-Airbus-SAFRAN property)[2]. The numerical setup is the same of the one presented in the second section of this paper. No motion are imposed on this computation because the objective is to compute the aerodynamic forces only induced by the distortion. The pressure on blade S_0 is extracted during the computation. The generalized aerodynamic force of mode i, $G^f_{af,i}(S_0)$, is computed by integrating the pressure on the blade projected on the 2-D complex modeshape ϕ_i as shown Eq. 20.

$$G^f_{af,i}(S_0,t) = -\iint_{S_0} P(t)(\overline{\underline{\phi_i}}(S_0).\underline{n})dS \tag{20}$$

The harmonic generalized aerodynamic force for the mode i and the nodal diameter N_D on the whole row, $\hat{G}^{f,N_D}_{af,i}$, are obtained with the Eq. 19. This new computation is needed for computing the generalized aerodynamic forces induced by the distortion for different modes and nodal diameters.

The 4^{th} first harmonic of the pressure fluctuations are illustrated in Fig. 11. The ground vortex induced strong fluctuations near the leading edge in the suction side. The levels are higher for the first harmonic and decrease for the upper harmonics. It is interesting to notice that the fluctuation are present on all the span of the blade. The pressure fluctuation seems then more correlated to the swirl angle distortion (Fig. 3) than the total pressure distortion which is more localized in upper part of the blade (Fig. 2).

Results

In order to evaluate the capacity of the model to predict the aerodynamic forces, a specific post-process is done for computing the radial distribution of dF_{aero}.

[1] In order to be more precise, all the harmonics corresponding to the ZigZag diagram should be taken into account, however higher harmonic levels ($N_{aube} - N_D, N_{aube} + N_D ...$) are very low compared to the first one corresponding to nodal diameter N_D.

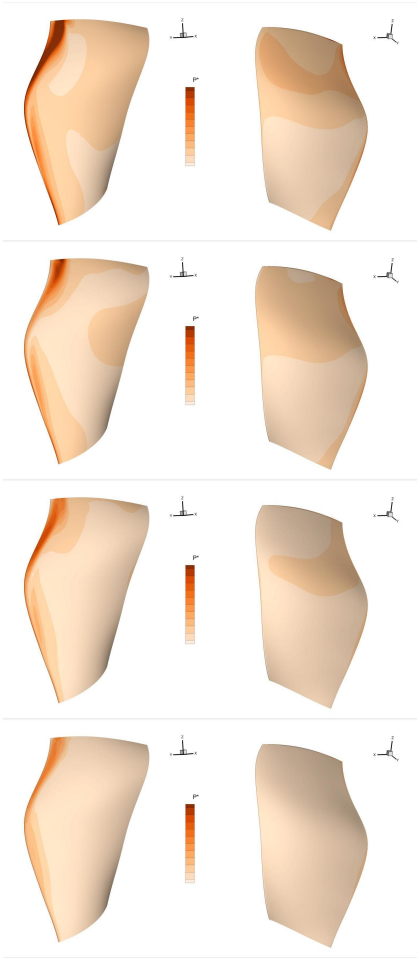

Figure 11: AMPLITUDE OF PRESSURE FLUCTUATION FOR THE FIRST FOURTH ENGINE ORDER (*left* : suction side, *right* : pressure side, *from the top to the bottom* : 1,2,3 and 4 EO).

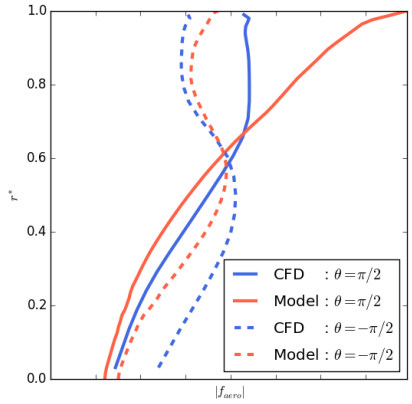

Figure 12: COMPARISON OF AERODYNAMIC FORCES DISTRIBUTION AT TWO AZIMUTHAL POSITIONS.

The comparison between CFD results and model results are presented in Fig. 12 for two different azimuthal positions of the blade S_0. The first position is $\theta = \pi/2$, when the blade is "far" from the vortex distortion, and the second position is $\theta = -\pi/2$, when the blade is "inside" the vortex distortion (cf Fig. 3). At both positions, the model slightly underestimates the aerodynamic force for low radius ($r^* < 0.65$) and overestimates for the high radius ($r^* > 0.65$). However, the evolution between the two positions is well captured by the model. Indeed, the vortex distortion leads to a decrease in angle of attack for the high radius, and therefore, a decrease in aerodynamic force. The opposite behavior is observed for the lower radius, the vortex induces an increase in angle of attack and therefore an increase in aerodynamic forces. All the distribution has changed between these two positions which indicates that the vortex impacts all the radius of the blade. This shows that the total pressure loss presented in Fig. 2, which is very localized at high radius, is not sufficient to explain the evolution in blade forces, which seems to be more depending on the swirl distribution.

In this section, the generalized aerodynamic forces are computed for the first three modes : 1F, 2F and 1T. For each mode, the first 4 nodal diameters are considered. The response at the 2F-4/rev crossing is principally driven by the 2F mode with the nodal diameter 4, however, the objective here is not to compute the forced response but to evaluate the ability of the model to compute the generalized aerodynamic forces due to a vortex ingestion. Fig. 13 represents the module of the harmonic generalized aerodynamic forces for the three modes considered. For each mode, the first four nodal diameters are presented. For the first bending mode (1F) and the second bending mode (2F), the conclusions are the same. First, the model overestimates generalized aerodynamic forces, this is probably because aerodynamic forces are overestimated at high radii (cf Fig. 12) where the displacement of the mode is the stronger. Second, the effect

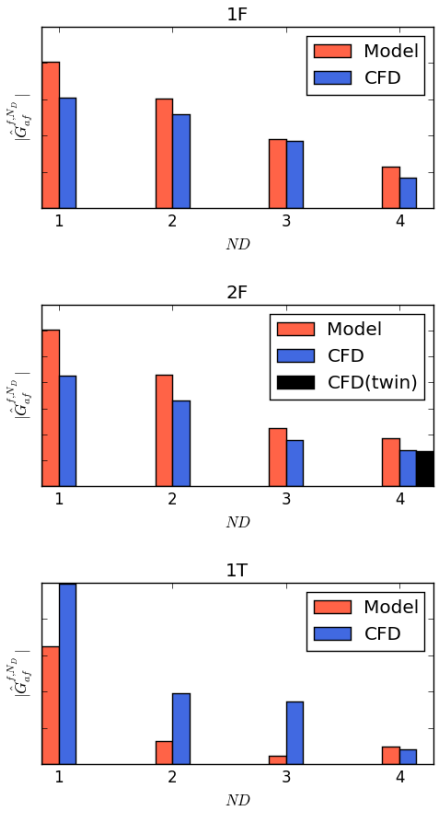

Figure 13: COMPARISON OF HARMONIC GENERALIZED AERODYNAMIC FORCES OF 1F, 2F AND 1T MODES FOR DIFFERENT NODAL DIAMETER.

of the nodal diameter is well captured by the model. For second bending mode with the nodal diameter 4, the value extracted from the two twin computations are also illustrated and shows very good agreement with the value extracted for the CFD computation without motion. This validates the superposition and linear assumptions made for the aero-mechanical analysis in the range of amplitudes evaluated. For the torsion mode(1T), the G^f_{af} levels are underestimated although the aerodynamic forces are overestimated, this is probably due to the reduction of the mode to its value in the quarter-chord line, which is close to the nodal line. It will be interesting to evaluate the mode in the leading edge, where the pressure fluctuations are the higher.

Considering the strong assumptions made in this model, the results show a remarkable agreement with high-fidelity computations for the bending modes. This again suggests that the forced response due to inlet ground vortex is principally driven by the swirl distortion.

CONCLUSION AND PERSPECTIVES

The objective of this paper was to investigate the dynamic response induced by the inlet ground vortex in resonance condition on large civil turbofan. The first step was to characterize the aerodynamic distortion induced by the ground vortex. A 3D-RANS computation was made on a large civil turbofan. The analysis of the flow field inside the intake shows that the vortex is responsible for a total pressure loss at the vortex core in a very localized area and positive and negative swirl angles impacting a large radial area. The second step was to compute the vibration levels at the 2F-4/rev crossing with a decoupled approach. This approach, based on superposition principle and linear aerodynamic behaviour, was used with two twin calculations with different prescribed harmonic motions. The aerodynamic excitation forces due to distortion and the aerodynamic response due to blade motion are then obtained through the analysis of generalized aerodynamic forces from both twin calculations. Results obtained are in good agreement with experimental results even though the level is slightly overestimated. And finally, a low-fidelity model based on the swirl distortion map and blade geometric features is proposed in order to compute the aerodynamic forcing due to the vortex on the first three modes and different nodal diameters. Comparisons to high-fidelity computations show relative good agreement for bending modes. The effect of the nodal diameter is well captured even though the levels are overestimated. Considering the strong assumptions of the model, this results suggest that the forced response due to inlet ground vortex is principally driven by the swirl distortion. Such a model could be helpful in preliminary design phases in order to quickly and roughly evaluate the forced response levels due to vortex ingestion.

The next step will consist of evaluating the model for different working points and distortions. Another aspect will be to take into account the non-linear behaviour of the structure coming from blade-disk contact [14]. Furthermore, an unsteady calculation including intake, ground and fan will be addressed in order to get rid of the boundary injection condition in fan calculations. This computation will be able to capture the unsteady ground vortex nature and a potential aerodynamic coupling between the fan and the ground vortex.

ACKNOWLEDGMENTS

The present study has been done thanks to the support of Safran Aircraft Engines.

References

[1] Thomas Berthelon, Alain Dugeai, Jonathan Langridge, and Fabrice Thouverez. Ground effect on fan forced response. In *15 International Symposium on Unsteady Aerodynamics, Aeroacoustics & Aeroelasticity of Turbomachines ISUAAAT15*, Oxford, UK, September 2018.

[2] Laurent Cambier, Sebastien Heib, and Sylvie Plot. The Onera elsA CFD software: input from research and feedback from industry. *Mechanics & Industry*, 14(3):159–174, 2013.

[3] Mauro Carnevale, Jeffrey S. Green, and Luca Di Mare. Numerical studies into intake flow for fan forcing assessment. In *ASME Turbo Expo 2014: Turbine Technical Conference and Exposition*, pages V01AT01A019–V01AT01A019. American Society of Mechanical Engineers, 2014.

[4] F. De Siervi, H. C. Viguier, E. M. Greitzer, and C. S. Tan. Mechanisms of inlet-vortex formation. *Journal of Fluid Mechanics*, 124:173–207, 1982.

[5] Luca di Mare, George Simpson, and Abdulnaser I. Sayma. Fan forced response due to ground vortex ingestion. In *ASME Turbo Expo 2006: Power for Land, Sea, and Air*, pages 1123–1132. American Society of Mechanical Engineers, 2006.

[6] A. Dugeai, Yann Mauffrey, and Frederic Sicot. Aeroelastic capabilities of the elsA solver for rotating machines applications. Paris, June 2011.

[7] J. S. Green. Forced response of a large civil fan assembly. In *ASME Turbo Expo 2008: Power for Land, Sea, and Air*, pages 685–692. American Society of Mechanical Engineers, 2008.

[8] R Henry. Calcul des frequences et modes des structures repetitives circulaires. *Journal mcanique applique*, 4(1):61–82, 1980.

[9] HD Li and L He. Single-passage analysis of unsteady flows around vibrating blades of a transonic fan under inlet distortion. *Journal of turbomachinery*, 124(2):285–292, 2002.

[10] J. G. Marshall and M. Imregun. A review of aeroelasticity methods with emphasis on turbomachinery applications. *Journal of fluids and structures*, 10(3):237–267, 1996.

[11] Ivan Mary. *Methode de Newton approche pour le calcul d'ecoulement instationnaires comportant des zones a tres faibles nombres de Mach.* PhD thesis, Universit Paris Sud, 1999.

[12] S. Moffatt and L. He. On decoupled and fully-coupled methods for blade forced response prediction. *Journal of Fluids and Structures*, 20(2):217–234, February 2005.

[13] John Murphy. Intake ground vortex aerodynamics. 2008.

[14] S Nacivet, C. Pierre, F. Thouverez, and L Jezequel. A dynamic Lagrangian frequencytime method for the vibration of dry-friction-damped systems. *Journal of Sound and Vibration*, 265(1):201 – 219, July 2003.

[15] A. Placzek. Aeroelastic damping predictions for multistage turbomachinery applications. In *ICAS 201429th Congress of the International Council of the Aeronautical Sciences*, 2014.

[16] LA Rodert and FB Garrett. Ingestion of foreign objects into turbine engines by vortices. *NACA*, TN(3330), February 1955.

[17] Stefan Schmitt, Volker Carstens, and Dirk Nrnberger. Evaluation of the principle of aerodynamic superposition in forced response calculations. *Unsteady Aerodynamics, Aeroacoustics and Aeroelasticity of Turbomachines*, page 133, 2006.

[18] H. W. Shin, E. M. Greitzer, W. K. Cheng, C. S. Tan, and C. L. Shippee. Circulation measurements and vortical structure in an inlet-vortex flow field. *Journal of Fluid Mechanics*, 162:463–487, 1986.

[19] D. L_ Thomas. Dynamics of rotationally periodic structures. *International Journal for Numerical Methods in Engineering*, 14(1):81–102, 1979.

[20] R Allan Wallis. *Axial Flow Fans: design and practice*. Academic Press, 2014.

[21] S. Zantopp, D. MacManus, and John Murphy. Computational and experimental study of intake ground vortices. *The Aeronautical Journal*, 114(1162):796–784, December 2010.